All solid-state lithium-ion batteries based on designed polyrotaxane-containing networks

Shanshan Yan [a], He Jia [a,*], Yanzhao Li [a], Zehan Chen [a], Rowanne Lyons [a], Zhenni He [a], Yinghui Zhang [a], Changwei Liu[b], Charles-André Fustin [a], Jean-François Gohy [a,*]

[a] Institute of Condensed Matter and Nanoscience (IMCN), Bio- and Soft Matter (BSMA), Université catholique de Louvain, Place L. Pasteur 1, 1348, Louvain-la-Neuve, Belgium

[b] Institute of Petro chemistry, Heilongjiang Academy of Science, Harbin 150040, China

Abstract

Selecting the appropriate polymer structure for use as both a solid electrolyte and catholyte is essential for enhancing the electrochemical performance of all-solid-state lithium metal batteries. In this study, we are pioneering the customization of solid electrolyte and catholyte synthesis based on novel polyrotaxane (PRX)-containing polymer networks by altering the length of the polyether crosslinkers to tune the properties to meet specific needs of different components. On one hand, the modified PRX polymer networks based on the shorter crosslinker show good mechanical strength, high ionic conductivity (7.25×10^{-4} S cm^{-1}) and high lithium ions transference number (0.54) at 60 °C, allowing their use as solid polymer electrolyte (SPE) self-supporting membranes. On the other hand, all-solid-state lithium-ion batteries with this SPE demonstrate a much higher initial capacity (above 160 mAh g^{-1} using $LiFePO_4$ as active material at the cathode and lithium metal as anode), and better cycling performance when paired with longer cross-linked PRX as catholytes than the other non-customized combinations all solid lithium-ion batteries. Moreover, the cycling performance of the full cell can be further improved by incorporating different lithium salts in the electrolyte (LiTFSI) and cathode ($LiClO_4$). This work highlights that the customized design of solid electrolytes and catholytes based on polymer networks is an efficient strategy to obtain high-performance all-solid-state lithium metal batteries.

Keywords

Modified polyrotaxane polymer networks, solid polymer electrolyte, catholyte, all-solid-state lithium-ion batteries

1. Introduction

Lithium-ion batteries (LIBs) have been considered as one of the most important energy storage systems since being introduced into the marketplace by Sony in 1991, which enable portable electronics, household appliances and electric mobility.[1] However, poor thermal stability, flammability, leakage and limited energy density have gradually become the bottlenecks for development of LIBs based on traditional liquid electrolytes.[2] Compared to conventional liquid electrolytes, solid electrolytes are safer and more compatible with high-voltage cathode materials and lithium metal anode.[3-5] The current research efforts on solid electrolytes are mainly focused on inorganic materials, polymer materials and composite systems.[6-8]

Compared to inorganic electrolytes, solid polymer electrolytes (SPEs) have outstanding advantages such as high flexibility and processing easiness.[9-11] Moreover, their structure can be easily tuned thanks to macromolecular design to satisfy performance requirements for all-solid-state lithium metal battery. However, the limited ionic conductivity at room temperature restricts the application of SPEs in all-solid-state lithium metal batteries.[12]

Among the different available families of polymer materials, polyrotaxanes (PRXs) belong to mechanically interlocked architectures and consist of a linear (polymer) chain on which is threaded a given amount of small cyclic molecules which can slide and rotate freely along the linear thread without chemical bonding restrictions. The cyclic molecules are prevented from de-threading by two bulky groups on the ends of the polymer thread.[13] Such mechanically interlocked architectures can restrict the crystallization of the polymer thread as well as promote the overall internal mobility in the material. At the same time, functional groups (if any) on the cyclic molecules provide interesting possibilities for further chemical modification. Those unique

features have motivated researchers to consider PRXs in SPEs. In this respect, Chen and coworkers first proposed SPEs based on PRXs composed of multiple α-cyclodextrins (α-CDs) cyclic molecules threaded on a linear poly(ethylene glycol) (PEG) chain. Due to this interlocked structure, the α-CDs effectively inhibited the crystallization of PEG. They also demonstrated that the nanochannels formed by α-CDs provided pathways for the directional motion of Li^+ and prevented the access of the anions by size exclusion, which could facilitate the Li^+ transport and improve the conductivity (10^{-6} S cm^{-1} at room temperature).[14] In order to improve the ionic conductivity in SPEs, other methods were used to modify PRXs such as grafting linear poly (ε-caprolactone) (PCL) side chains,[15] crosslinking[16] and combining poly(vinylidene fluoride-*co*-hexafluoropropylene)-grafted PRXs with nano-Al_2O_3 particles.[17]

In addition to the solid electrolytes, the performance of all-solid-state batteries is also affected by the utilization of active materials in the cathode. Indeed, without the infiltration of liquid electrolytes, wetting of the cathode active material by the so-called catholyte is required in order to obtain physical contact between the different components in the cathode and allow Li^+ transport inside the cathode and at the interface between the cathode and the solid electrolyte.[18] However, the research field on catholytes for all-solid-state lithium metal batteries is still in its infancy. At present, the most commonly used method is incorporating PEO based catholyte into the cathode, the amount of PEO based catholyte is around 40 %.[19-23]

Selecting the suitable polymer material to be used both as SPE and catholyte is crucial for improving the electrochemical performance of all-solid-state lithium-ion batteries.[24] In this contribution, we propose a novel PRX-based polymer network whose structural parameters could be easily varied in order to meet requirements of both the SPE and catholyte for further utilization

in an all-solid-state lithium metal battery. Our design is based on a PRX consisting of a PEG chain and threaded α-CDs rings. The novel polymer network is further formed by reacting the hydroxyl groups on the α-CDs rings with epoxy groups of PEG diglycidyl ethers of different chain lengths. This strategy allows the formation of a polymer network in which the crosslinking nodes are not immobilized but can move along with the rings.[25, 26] Such an approach, beside the tunability due to the variation of the length of the PEG diglycidyl ether crosslinker, is believed to limit the crystallization behavior of PEG and to increase the mobility of Li^+ ions because of the continuous reconfiguration of the network due to the α-CDs rings. The corresponding SPE based on modified PRX polymer network exhibits good mechanical strength, high ionic conductivity (7.25×10^{-4} S cm^{-1}) and wide electrochemical stability window as well as high lithium ions transference number (0.54) at 60 °C. Moreover, compared with traditional PEO based catholyte, the all-solid lithium-ion batteries with longer cross-linking PRX as catholyte significantly improves the initial discharge capacity and achieves 98.7 % of theoretical capacity as well as good long stability at 60 °C. More importantly, selecting different types of lithium salts based on the distinct performance requirements of the electrolyte (LiTFSI) and cathode ($LiClO_4$) can significantly improve long-term cycling stability under varying rate conditions (0.1C and 0.2C alternating cycling), even though the initial capacity may slightly decrease.

2. Experimental section

2.1 Materials

Poly(ethylene glycol) (PEG, M_n=35000 g mol^{-1}), Poly(ethylene oxide) (PEO, M_v=200000 and 600000 g mol^{-1}), Poly(ethylene glycol) diglycidyl ether (PEGDE, M_n=500 and 2000 g mol^{-1}),

dimethyl sulfoxide (DMSO, 99.5+%, for analysis) and 2,2,6,6-tetramethylpiperidine 1-oxyl (TEMPO) were purchased from Sigma-Aldrich. α-Cyclodextrin (α-CD content > 98.0%) was supplied by TCI Chemicals. Adamantan-1-amine and benzotriazol-1-yloxytris(dimethylamino)phosphonium hexafluorophosphate (BOP) were bought from Fluorochem. Sodium hydroxide and acetonitrile (ACN) were supplied by VWR. Lithium bis(trifluoromethanesulfonyl)imide (LiTFSI) and lithium perchlorate ($LiClO_4$) were purchased from Sigma-Aldrich. Lithium iron phosphate ($LiFePO_4$), multi-walled carbon nanotubes and super-p were acquired from TOB. N-methyl-2-pyrrolidone (NMP) was purchased from Fisher chemical. The chemicals used for synthesizing the polymers were reagent grade and the chemicals used for preparing the batteries were battery grade, all were used without further purification.

2.2 Synthesis of crosslinked polyrotaxanes

In a first step, a PRX based on PEG and α-CDs was prepared according to the literature.[27] Briefly, α-CDs were threaded on an α,ω-dicarboxylic acid functionalized PEG that was obtained by TEMPO oxidation of α,ω-dihydroxy PEG (see Figure 1a). Adamantamine stoppers were then grafted via a peptidic coupling reaction using BOP as coupling agent on the terminal carboxylic acid groups of the PEG thread to obtain the desired PRX. In a second step, crosslinked PRXs (CPRs) were prepared by reacting, in basic medium, hydroxyl groups on the α-CDs of the PRX with a α,ω-diepoxy functionalized PEG (PEGDE, see Figure 1a). As a typical example, 500 mg PRX were dissolved in 50 mL of 1 M aqueous NaOH. 14.5 mL PEGDE (M_n=500 g mol^{-1}, PEGDE: α-CDs=85:1 mol/mol) were dropwise added to the above solution, and the mixture was stirred at 50 °C for 20 h. Then, the mixture was dialyzed against Milli-Q water in a cellulose bag (MWCO = 13~14 kDa)

for 5 days and the Milli-Q water was changed 5 times. Then the mixture was freeze-dried to recover the CPR (designated as CPR500 because PEGDE with M_n=500 g mol^{-1} was used here). 3.6 PEGDE500 are attached on each α-CD when the ratio of PEGDE and α-CDs is 85:1. For the synthesis of CPR2000, 20 mg PRX were reacted with 300 mg PEGDE (M_n=2000 g mol^{-1}, PEGDE: α-CDs=10:1 mol/mol) in 2 mL of 1 M aqueous NaOH at 50 ℃ for 20 h. The purification process of CPR2000 is the same as that of CPR500.

2.3 Preparation of solid polymer electrolytes

Solid polymer electrolytes (SPEs) were obtained by mixing predetermined amounts of CPR500 or CPR2000 with $LiClO_4$ in order to obtain 8:1, 10:1,15:1 and 20:1 ether (EO) unit/Li^+ molar ratios, in which EO is from the PRX and PEGDE. For the typical example of the CPR500-$LiClO_4$ SPE with 10:1 EO/Li^+ molar ratio, 400 mg CPR500 and 52 mg $LiClO_4$ were separately dissolved in 3 and 1.5 mL DMSO under stirring for 24 h, respectively. Then, the two solutions were mixed for 48 h to prepare a homogeneous mixture at room temperature. The mixture was cast in a Teflon mold and dried under vacuum at room temperature for 5 days to remove most of the DMSO. Lastly, the sample was dried in a vacuum oven at 100 ℃ for 24 h to obtain the CPR500-$LiClO_4$ SPE with 10:1 EO/Li^+ molar ratio. The synthesis of CPR500-LiTFSI SPEs with 10:1 EO/Li^+ molar ratio is as same as that of CPR500-$LiClO_4$ ones. The synthesis of CPR2000-$LiClO_4$ SPEs is different from that of CPR500-$LiClO_4$ ones since a solvent-free approach was used. In a typical example, 30 mg CPR2000 and 4.32 mg $LiClO_4$ were mixed at 80 ℃ with no solvent for 1 h to obtain the CPR2000-$LiClO_4$ SPE with 15:1 EO/Li^+ molar ratio. PEO-based SPEs were also prepared as reference samples for comparison purpose. For the synthesis of the PEO-$LiClO_4$ SPE with 10:1

EO/Li^+ molar ratio, 500 mg PEO (M_v=200000 g mol^{-1}) and 120 mg $LiClO_4$ were dissolved in 2.5 and 1 mL ACN, respectively. After mixing the two solutions and further stirring for 24 h, the resulting solution was poured in a Teflon mold and most of solvent was removed at room temperature by evaporation. Then, the PEO-$LiClO_4$ SPE with 10:1 EO/Li^+ molar ratio was further dried in the oven at 80 ℃ for 24 h.

2.4 Preparation of the cathodes and cell assembling

The cathodes, designated as LFP2000 and LFP500, were made of 30 wt% $LiFePO_4$ (LFP), 20 wt% Super-P (SP), 10 wt% multi-walled carbon nanotubes (CNT) and 40 wt% CPR2000-$LiClO_4$ or CPR500-$LiClO_4$ as catholyte (the ratio based on the reported results in the literatures from Table S1 in the supporting information), respectively. The LFP2000-LiTFSI cathode was made of 30 wt% LFP, 20 wt% SP, 10 wt% CNT and 40 wt% CPR2000-LiTFSI as catholyte. A slurry was prepared by mixing at 2000 rpm for 30 min, in which 100 mg cathode components dispersed in 0.6 mL NMP, then the slurry was coated on a carbon-coated aluminum foil with a thickness of 100 mm and dried in a dynamic vacuum oven at 100 °C for 24 h. As a reference, PEO (M_v=600000 g mol^{-1}) is used in the LFP600K cathode. CR2032-type coin cells were assembled with LFP2000 (LFP500 or LFP600K) disks (diameter=10mm) as cathodes, CPR500-$LiClO_4$ as SPE and polished lithium metal foil as anode. CR2032-type coin cells were also assembled with LFP2000 (or LFP2000-LiTFSI) cathode (diameter=10mm), CPR500-LiTFSI as SPE and polished lithium metal foil as anode.

2.5 Material characterization

Nuclear magnetic resonance (NMR) spectroscopy was performed on a Bruker 300 UltraShield spectrometer with d6-DMSO as solvent. Fourier transform infrared spectroscopy (FTIR) was conducted on an Agilent Technologies Cary 630 FTIR with a Nicolet iN10 spectrometer using transmission mode method at room temperature in the range of 610~4000 cm^{-1} with a resolution of 4 cm^{-1} with 64 scans. Thermogravimetric analysis (TGA) of polymers was conducted on a Netzsch STA 449F3 with the heating rate of 10 °C min^{-1} from 30 °C to 800 °C. Differential scanning calorimetry (DSC) was performed with a Mettler Toledo DSC1 equipped with STARe software and the temperature was varied from –80 to 120 °C with a heating rate of 10 °C min^{-1} under nitrogen atmosphere. Small amplitude oscillatory shear (SAOS) measurements were carried out by using a MCR-301 (Anton Paar) rheometer. Samples were placed between stainless steel parallel plates with a diameter of 8 mm. The samples were equilibrated on the rheometer at 100 °C for 30 min under nitrogen atmosphere, and normal forces were checked to be relaxed prior to any measurement. Dynamic frequency sweep measurements were performed at different temperatures in the range from 0.1 to 100 rad s^{-1}. All dynamic measurements were performed in the linear viscoelastic region, which was determined from dynamic strain sweep tests. The surface morphology of the $LiFeO_4$ cathodes and Li anodes was examined by a Zeiss Auriga focused ion beam scanning electron microscope (FIB-SEM). Dynamic mechanical analysis (DMA) was performed on Mettler Toledo DMA/SDTA861 by the shear deformation mode, in which the viscoelasticity response of a sample under oscillating load was monitored over temperatures. A tube furnace (Nabertherm R 50/250/13 with Controller C450) was applied to calcine samples. X-ray photoelectron spectroscopy (XPS) was carried out using the SSI X-Probe (SSX 100/206)

photoelectron spectrometer from FISONS equipped with a monochromatized microfocus Al-Kα X-ray source.

2.6 Electrochemical measurements

Electrochemical impedance spectroscopy (EIS) was obtained at a voltage amplitude of 10 mV and frequency range from 7 MHz to 100 mHz. All the measurements were carried out from 90 to 20 °C by a programmed instruction on a Bio-Logic VMP-300 potentiostat. Linear sweep voltammetry (LSV) was measured on a Bio-Logic VMP-300 potentiostat with a scan rate of 1 mV s^{-1} at 60 °C. Lithium-ion transference number (t_{Li^+}) determination was carried out with an applied potential of 50 mV in a symmetric Li||CPR500-$LiClO_4$||Li cell on a Bio-Logic VMP-300 potentiostat. The galvanostatic cycling experiments were used to investigate the interface stability between the solid polymer electrolyte and the lithium metal anode. The symmetrical Li||CPR500-$LiClO_4$||Li and Li||PEO-$LiClO_4$||Li cells were charged and discharged repeatedly for 1 h with a constant current density of 0.025 mA cm^{-2} at 60 °C using a NEWARE battery testing system. The galvanostatic cycling experiments at different current densities from 0.01 to 0.10 mA cm^{-2} at 60 °C were also realized. Galvanostatic intermittent titration technique (GITT) measurements were performed on a NEWARE battery testing system. The cells were set to relax for 2 hours after every 30 min for discharging and charging at 0.1 C at 60 °C. The charge and discharge tests were carried on a NEWARE battery test system. The C-rate of LFP2000 (LFP500 or LFP600K)||CPR500-$LiClO_4$||Li was varied from 0.1 to 0.2, 0.5, 1 C and then back to 0.1 C at 60 °C. The long-term cycling stability test of LFP2000-$LiClO_4$||CPR500-$LiClO_4$||Li was performed at 0.1 C for 90 cycles at 60 °C. The cycling stability test of LFP2000-LiTFSI||CPR500-LiTFSI||Li was performed at 0.1 C

and 0.2 C for 55 cycles at 60 °C. The cycling stability test of LFP2000-$LiClO_4$||CPR500-LiTFSI||Li was performed at 0.1 C and 0.2 C for 90 cycles at 60 °C. The potential window was ranged from 3.0 to 3.8 V (*vs.* Li/Li^+). Charge and discharge rates were calculated based on the theoretical capacity of LFP (C=170 mA g^{-1}).

3. Results and discussion

Figure 1a schematically depicts the synthesis of novel designed polymer networks based on PRX. Firstly, a polyrotaxane is prepared, in which α-CDs rings are threaded onto a PEG linear chain end-capped at both ends with adamantan-1-amine stoppers. As evidenced in Figure S1, all characteristic peaks of the protons on PEG and α-CD from the inclusion complex (α-CDs/PEG-COOH) and the synthesized polyrotaxane were confirmed by ^1H NMR analysis. The signal peak around 3.51 ppm was attributed to the methylene of PEG. The chemical shifts of protons on α-CD appeared at 5.52 ppm (O2H), 5.45 ppm (O3H), 4.49 ppm (O6H), 4.80 (H1) and 3.85–3.20 ppm (H2,3,4,5,6). [28] Besides the characteristic peaks of PEO and α-CD, peaks at 2.01, 1.94, and 1.62 ppm were attributed to the protons of the carbon skeleton in adamantamine for polyrotaxane. [29] The comparison of the integrations of the characteristic peaks related to PEO and adamantamine reveals that the yield of the end-capping reaction is close to 100%, clearly demonstrating the successful formation of the PRX. According to the ^1H NMR spectrum shown in Figure S1, around 100 α-CDs are threaded on the PEG main chain of PRX, which corresponds to the result reported in the literature.[27] Then, two novel crosslinked polyrotaxanes, namely CPR500 and CPR2000, are formed by using a,ω-diepoxy PEG chains (PEGDEs with M_n=500 and 2000, respectively) as crosslinkers. The PEGDE crosslinking chains are reacted with the hydroxyl groups of α-CDs rings

on the PRX in basic medium in order to confer segmental mobility to the accordingly obtained networks (Figure 1a). The chemical shifts of PRX, CPR500 and CPR2000 were investigated by ^{1}H NMR analysis. As evidenced in Figure S2, strong NMR resonance peaks appeared in the range of 3.3 to 6.0 ppm, which were ascribed to the proton signals of α-CDs and ether functions for CPR500 and CPR2000.[30] A new signal (H7) with the chemical shift of 4.60 ppm was observed in both CPR500 and CPR2000 spectra, which results from the reaction between the epoxy rings of PEGDE and the hydroxyl groups (O2H, O3H and O6H) of the α-CDs rings on the PRX.[30, 31, 32, 33] The peaks of O2H and O3H of α-CDs became weaker and broader, and O6H experienced a small upfield shift (from 4.49 to 4.45 ppm), as compared with that in pure PRX. These results clearly demonstrated that the epoxy group of PEGDE interacts with hydroxyl group in the outer cavity of α-CDs. In addition, the characteristic signal of epoxy groups in the FTIR spectra, which can be observed at 912 cm^{-1} for PEGDE, disappears for CPR500 and CPR2000, further confirming the opening of the epoxy groups during the crosslinking reaction (Figure 1b).[34] In a further step, small amplitude oscillatory shear measurements have been performed in order to assess the mechanical properties of the formed CPR networks. Figure 1c compares the storage modulus (G′) and loss modulus (G″) measured at 60 °C for CPR500 and CPR2000, respectively. Both samples show a rubber-like viscoelastic behavior with G′ always superior to G″ in the investigated angular frequencies, suggesting that the targeted polyrotaxane-based networks were successfully formed. The values measured for G′ are proportional to the stiffness of the material.[35] The elastic modulus of CPR500 is higher compared to that of CPR2000, indicating a stiffer network for CPR500. This was also confirmed by frequency sweep tests for the CPR500 and CPR2000 networks at different temperatures as shown in Figure S3. Those results are not surprising since the

crosslinking density of the CPR500 network is expected to be larger than the one of the CPR2000 network, in direct relation to the length and amount of the PEGDE crosslinker. This explains why a stiffer network is observed for CPR500 compared to CPR2000.

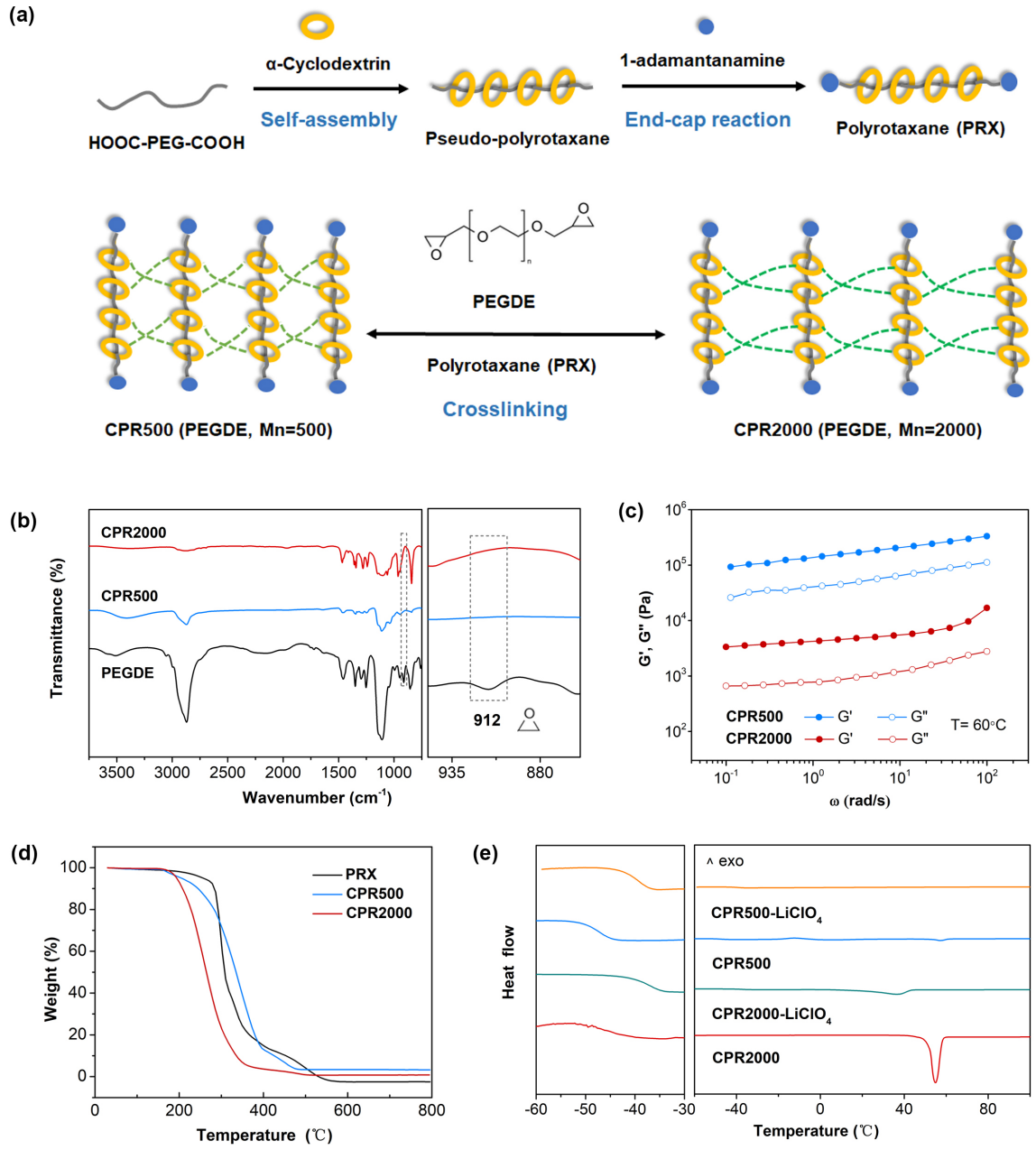

Figure 1. (a) Synthesis of polyrotaxane (PRX) and novel crosslinked polyrotaxanes (CPR500 and CPR2000) with PEGDE (Mn=500 or 2000) as crosslinker. (b) FTIR spectra of PEGDE, CPR500 and CPR2000. (c) Dynamic

frequency sweep curves of CPR500 and CPR2000 at 60 °C. (d) TGA of PRX, CPR500 and CPR2000. (e) DSC curves of CPR500, CPR500-$LiClO_4$ (EO: Li^+=10:1), CPR2000 and CPR2000-$LiClO_4$ (EO: Li^+=15:1).

TGA and DSC measurements were used to investigate thermal properties of novel polymer networks based on polyrotaxane. As shown in Figure 1d, the starting PRX, CPR500 and CPR2000 exhibit high thermal stability with degradation occurring around 200 °C. DSC thermograms are plotted in Figure 1e and allow the determination of the glass transition (T_g) and melting temperature (T_m) of the networks. In our networks, crystallinity is solely originating from the PEG segments of the crosslinker since the PRX does not show a melting peak (Figure S4). Therefore, the crystallinity degree of the networks has been determined by integrating the melting peak and comparing the obtained value to the melting enthalpy of pure PEG crystalline domains ($\triangle H_m$ = 202.41 J g^{-1}).[36] As expected, with the increasing chain length of the PEGDE crosslinker, the crystallinity of the networks increased (0% for PRX, 2.1% for CPR500 and 86.0% for CPR2000, Figure S4 and Figure 1e). Crystallinity has a detrimental effect on the mobility of Li^+ ions but can be also strongly influenced by the addition of salt, being either decreased or increased depending on the salt loading and salt nature.[37] In this respect, the crystallinity degree has been also measured for CPR networks loaded with $LiClO_4$ salt, including CPR500-$LiClO_4$ (EO: Li^+=10:1) and CPR2000-$LiClO_4$ (EO: Li^+=15:1) (Figure 1e), which are the samples showing the highest conductivity (see below). Obviously, the presence of $LiClO_4$ into the networks at these salt loadings inhibits the crystallization in CPR500 and CPR2000 (0% for CPR500-$LiClO_4$ and 34.7% for CPR2000-$LiClO_4$). The T_m of CPR500 and CPR2000 are 57.6 and 54.8 °C, while CPR500-$LiClO_4$ does not show a melting peak and CPR2000-$LiClO_4$ shows a T_m of 37.2 °C. Finally, low T_g values of –48.1 °C and –49.6 °C have been measured for the CPR500 and CPR2000 networks, respectively,

in coherence with the high flexibility of PEG.[38] Low T_g values are also observed for the salt-loaded CPR500-$LiClO_4$ and CPR2000-$LiClO_4$ samples, although higher than for the samples without $LiClO_4$. Low crystallinity and low T_g values in lithium salt loaded CPR networks are very positive for the further utilization of those samples as SPEs and catholytes. The mechanical properties of solid polymer electrolyte CPR500-$LiClO_4$ (EO: Li^+=10:1) and the polymer CPR500 were studied by linear shear rheology. Typically, the mechanical properties of solid polymer electrolytes decrease with the addition of lithium salts because the salt acts as a plasticizer for the polymers.[39] Figure S5a-c shows the rheological data obtained for CPR500 and CPR500-$LiClO_4$. Frequency sweeps have been measured for two samples in the temperature range from 100 to 60 °C in the linear viscoelastic regime. It is clearly observed that G′ decreases when $LiClO_4$ is added to CPR500, confirming the plasticizing effect of $LiClO_4$. Furthermore, this leads to a significant decrease in the crystallinity of the CPR500-$LiClO_4$, which is evidenced from the DSC curves in Figure S5d. The storage modulus of CPR500 and CPR500-$LiClO_4$ decreases with increasing temperature, which can be attributed to the higher mobility of polymer chain segments and the dynamic hopping of ions between polymer chains. [40, 41]. The mechanical properties of the electrolyte have been studied by DMA in the shear deformation mode, as shown in Figure S6. In the low-temperature region (up to about -20°), the solid polymer electrolyte CPR500-$LiClO_4$ (EO: Li^+=10:1) shows high shear storage modulus around 10^6 Pa. Above room temperature, the modulus of the electrolyte still remains around 10^5 Pa. In the next step, the ionic conductivity in those samples will be assessed (Figure 2).

Ionic conductivity is an important parameter for selecting solid polymer electrolytes with superior electrochemical performance for all-solid-state lithium battery. As shown in Figure 2a,

the ionic conductivities of CPR500-$LiClO_4$ samples with various EO/Li^+ molar ratios were explored via electrochemical impedance spectroscopy at temperatures ranging from 90 to 20 °C. The variation of the ionic conductivity is mainly due to the varying amount of the charge carrying ions.[16] In this respect, the best performance has been observed with the EO/Li^+ molar ratio of 10:1, with conductivities of 2.60×10^{-3} and 7.25×10^{-4} S cm^{-1} at 90 and 60 °C, respectively. This optimal EO/Li^+ molar ratio is in agreement with previously published results for PEO-based SPEs.[42] At room temperature, the CPR500-$LiClO_4$ sample with an EO/Li^+ ratio of 10:1 also shows a higher ionic conductivity (1.88×10^{-5} S cm^{-1}) than that of PEO-$LiClO_4$ sample (1.60×10^{-8} S cm^{-1}).[43] It is generally acknowledged that high amounts of added lithium salts lead to salt clusters which are detrimental to the ionic conductivity.[44, 45] Table S2 summarizes the electrochemical performance of solid electrolytes based on the (pseudo)polyrotaxanes, including ionic conductivity (σ), lithium ion transference number (t_{Li^+}) and electrochemical stability window (ESW). The dissociation of the lithium salt in the solid polymer electrolyte is critical for its performance in all-solid-state batteries, and can be visualized here by the interaction between lithium ions and the ether groups (EO, C-O-C).[46] However, lithium ions could also interact with ether oxygens in the glucose unit of α-CDs which renders the quantification of the Li^+/EO groups interactions difficult in our samples because of wide peaks in the corresponding regions of the FTIR spectra (Figure 2b).[47] Besides the signals assigned to Li^+/EO groups, FTIR peaks associated to the ClO_4^- anions are also sensitive to their dissociation degree. In this respect, perchlorate anions are expected to interact with the hydroxyl groups of α-CDs through hydrogen bonding, further promoting the dissociation of lithium salts and freeing more Li^+ ions.[47] Therefore, the local environment of ClO_4^- in the CPR500-$LiClO_4$ SPE with different EO/Li^+ molar ratios has been

investigated by FTIR spectroscopy. In FTIR spectra, the dissociation of $LiClO_4$ is visible in the wavenumber range of 610–650 cm^{-1}. Specifically, the peak at ~624 cm^{-1} is assigned to the dissociated free ClO_4^- anion and the peak around ~635 cm^{-1} corresponds to the contact $Li^+ClO_4^-$ ion pair.[48] The comparison between these two peaks allows the determination of the dissociation ratio of $LiClO_4$ salt in the SPE. The Gaussian–Lorentzian fitting results for CPR500-$LiClO_4$ FTIR spectra with different EO/Li^+ molar ratios are shown in Figure 2c and Table S3 summarizes the simulated dissociation ratios for the CPR500-$LiClO_4$ sample. The dissociation ratio (84.2%) at 10:1 EO/Li^+ molar ratio is higher than that of other ratios.

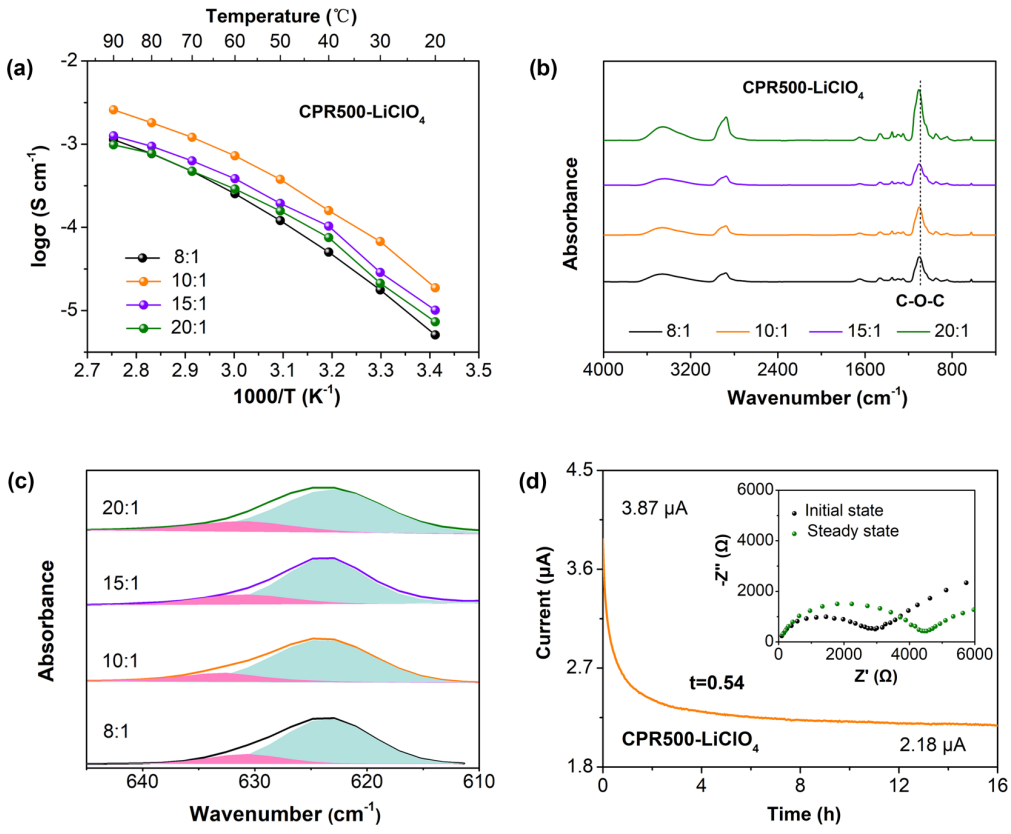

Figure 2. (a) Arrhenius plots of the ionic conductivity for CPR500-$LiClO_4$. (b) FTIR spectra of CPR500 and CPR500-$LiClO_4$ in the range of 610–4000 cm^{-1}. (c) FTIR spectra at 610–645 cm^{-1} and corresponding

Gaussian–Lorentzian fitting of the ClO_4^- absorbance for CPR500-$LiClO_4$. (d) Polarization curve, initial (in black) and steady state (in green) impedance diagram (inset) for CPR500-$LiClO_4$ (10:1) at 60 °C.

To confirm the hydrogen bonding interactions between ClO_4^- anions and hydroxyl groups in the investigated SPEs and their beneficial effect of lithium salt dissociation and Li^+ mobility, the ionic conductivities of CPR500 loaded with $LiClO_4$ and LiTFSI at the same EO/Li^+ molar ratio have been compared. In Figure 3a, the ionic conductivity of CPR500-$LiClO_4$ is higher than that of CPR500-LiTFSI at 10:1 EO/Li^+ molar ratio, which could result from the strong hydrogen bonding between hydroxyl groups of α-CDs and ClO_4^-. The associated high binding energy is related to the salt dissociation, which results in a large amount of free Li^+ ions.[47] Figure 3b shows the VFT plots of CPR500-$LiClO_4$ and CPR500-LiTFSI at 10:1 EO/Li^+ molar ratio. The activation energy of CPR500-$LiClO_4$ is lower than that of CPR500-LiTFSI, which leads to higher ionic mobility and conductivity. This last measurement definitely confirms that ClO_4^- anions are strongly interacting with hydroxyl groups in the CPR samples, further freeing Li^+ ions at the benefit of the overall ionic conductivity. Finally, an optimal EO/Li^+ molar ratio of 10:1 has been determined for CPR500-$LiClO_4$. The lithium-ion transference number (t_{Li^+}) is another crucial parameter to characterize the electrolyte performance. Figure 2d shows the time-dependent response of a Li||CPR500-$LiClO_4$||Li symmetric cell and the inset depicts the electrochemical impedance spectroscopy (EIS) signal in the initial state and steady state. Due to a large amount of free Li^+ ions, the t_{Li^+} for the CPR500-$LiClO_4$ is calculated to be 0.54 at 60 °C, which exceeds that of linear PEO-$LiClO_4$ electrolytes (t_{Li^+}=0.1~0.3) [49, 50], and confirms that strong interactions between perchlorate anions and hydroxyl groups in the investigated SPEs are able to free Li^+ ions and make them available for transport through the electrolyte membrane.

As shown in Figure S6, the ionic conductivities of CPR2000-$LiClO_4$ SPEs with different molar ratios of EO and Li^+ have been also studied. The CPR2000-$LiClO_4$ sample shows ionic conductivity values of 7.31×10^{-4} and 3.13×10^{-4} S cm^{-1} at 90 and 60 °C at 15:1 EO/Li^+ molar ratio, respectively, which are lower than that of CPR500-$LiClO_4$ with the 10:1 EO/Li^+ molar ratio (see Figure 3c). This could be related to the crystallinity of CPR2000-$LiClO_4$ compared to the almost fully amorphous CPR500-$LiClO_4$ sample. This is further confirmed by the change of slope in the ionic conductivity *vs* temperature curve noted around T_m (37.2 °C) for the CPR2000-$LiClO_4$ sample in the range of 30–60 °C. Obviously, conductivity values for CPR2000-$LiClO_4$ are decreasing more sharply below T_m. However, the ionic conductivity of CPR2000-$LiClO_4$ (8.53×10^{-5} S cm^{-1} at 30 °C) is much higher than that of PEO-$LiClO_4$ (7.33×10^{-7} S cm^{-1} at 30 °C) at the same EO/Li^+ molar ratio of 15:1,[51] clearly demonstrating the superiority of the polyrotaxane-based networks developed here. According to the literature, there should be two possible pathways for transferring lithium ions in our system, the nanochannels formed by self-assembly of PEO and α-CD and the side chains grafted on the α-CD.[14, 15] The lower ionic conductivity of CPR2000-$LiClO_4$, compared with CPR500-$LiClO_4$, results from the crystallization of the longer side chains, as indicated by DSC, which proves that the lithium ion transport mainly relies on the side chains. The fast molecular motion of short PEGDE side chains contributes to the high ionic conductivity. Linear sweep voltammetry was finally used to determine the electrochemical stability window of solid polymer electrolytes. As shown in Figure 3d, the CPR500-$LiClO_4$ and CPR2000-$LiClO_4$ show a wide electrochemical stability window from 1.6 to 4.8 V (*vs.* Li^+/Li) with a scan rate of 1 mV s^{-1} at 60 °C.

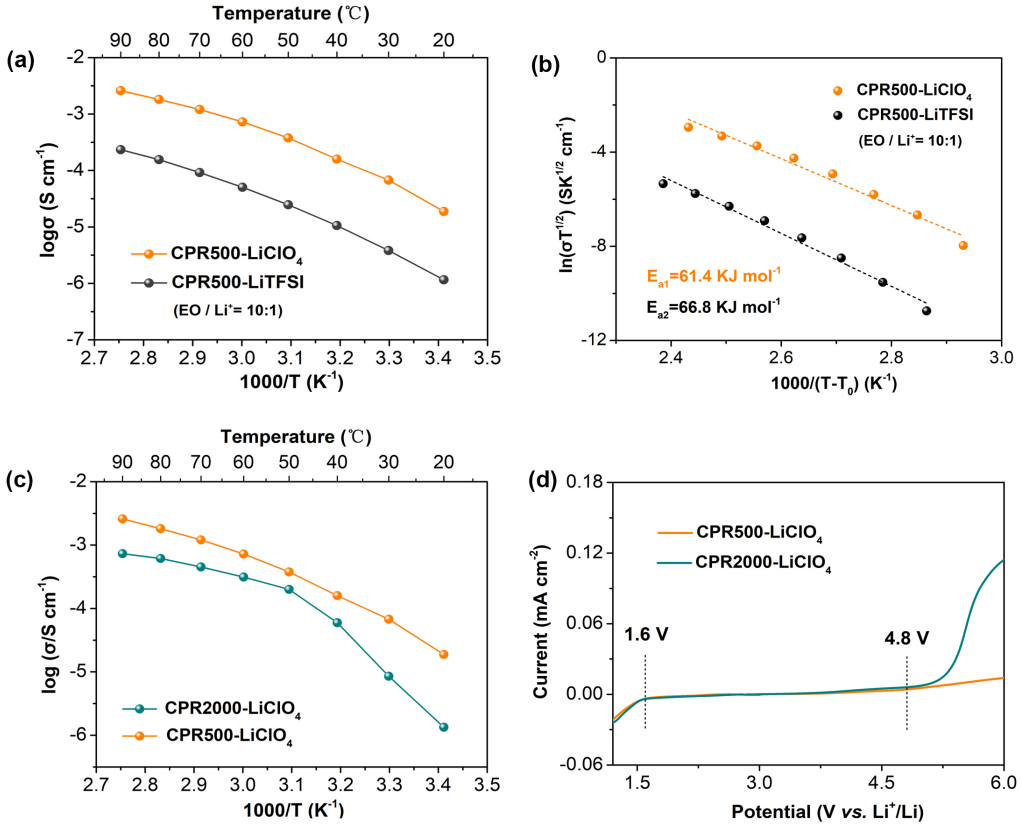

Figure 3. (a) Arrhenius plots of the ionic conductivity for CPR500-$LiClO_4$ and CPR500-LiTFSI. (b) Vogel–Tammann–Fulcher (VFT) fitting plots for CPR500-$LiClO_4$ and CPR500-LiTFSI. (c) Comparison of ionic conductivity of CPR500-$LiClO_4$ (10:1) and CPR2000-$LiClO_4$ (15:1). (d) Linear sweep voltammograms for CPR500-$LiClO_4$ (10:1) and CPR2000-$LiClO_4$ (15:1) at 60 °C with a scan rate of 1 mV s^{-1}.

Since the CPR500-$LiClO_4$ sample with 10:1 EO/Li^+ molar ratio was the sample exhibiting the best ionic conductivity whatever the temperature, it was further investigated for use as SPE in all-solid-state battery prototypes. However, before performing battery testing, the interfacial stability between the CPR500-$LiClO_4$ SPE and lithium metal needs to be tested by galvanostatic cycling experiments. Figure 4a shows the voltage profiles of Li||CPR500-$LiClO_4$||Li and reference Li||PEO-$LiClO_4$||Li symmetrical cells at the current density of 0.025 mA cm^{-2} at 60 °C. The Li||CPR500-$LiClO_4$||Li symmetric cell can run for 300 h, while the Li||PEO-$LiClO_4$||Li symmetric cell suffers

from hard short after 165 h.[52] In comparison to the Li||PEO-$LiClO_4$||Li symmetric cell, the Li||CPR500-$LiClO_4$||Li cell shows lower initial and final overpotentials (38 mV and 52 mV), indicating a better interfacial stability between CPR500-$LiClO_4$ and lithium metal compared to PEO-$LiClO_4$. The cycling stabilities of Li||PEO-$LiClO_4$||Li and Li||CPR500-$LiClO_4$||Li cells at various current densities have been then studied. As illustrated in Figure 4b, the Li||PEO-$LiClO_4$||Li shows hard short when the current density is reaching 0.03 mA cm^{-2}, while the Li||CPR500-$LiClO_4$||Li cell exhibits stable overpotentials at current densities ranging from 0.01 to 0.05 mA cm^{-2} for 50 h at 60 °C. The Li||CPR500-$LiClO_4$||Li cell exhibits lower overpotential than the Li||PEO-$LiClO_4$||Li cell at same current densities, demonstrating that the CPR500-$LiClO_4$ SPE shows a better interfacial stability with lithium metal. Impedance measurements of Li||CPR500-$LiClO_4$||Li cell at different current densities from 0.01 to 0.05 mA cm^{-2} at 60 °C have also been carried out, as shown in Figure 4c. The Li||CPR500-$LiClO_4$||Li cell exhibits two semicircles. The first semicircle in the higher frequency range indicates the resistance of the solid polymer electrolyte while the second semicircle in the lower frequency range represents the charge transfer resistance (R_{ct}) between the solid polymer electrolyte and the lithium metal.[53] The two resistances determined for this cell show a little change from 0.01 to 0.05 mA cm^{-2}, which illustrates that the CPR500-$LiClO_4$ has superior interfacial stability against lithium metal. Scanning electron microscopy (SEM) was used to further investigate the stability between CPR500-$LiClO_4$ and lithium metal. Figure 4d shows the surface morphologies of the fresh Li and the Li anodes from Li||PEO-$LiClO_4$||Li and Li||CPR500-$LiClO_4$||Li cells after running for 300 h at the current density of 0.025 mA cm^{-2}. A smooth surface is observed for fresh lithium. The Li anode from the Li||PEO-$LiClO_4$||Li cell exhibits massive lithium dendrites and non-uniform Li deposition, while a

flat surface is observed on the surface of the Li anode from Li||CPR500-$LiClO_4$||Li cell. The above results clearly indicate that CPR500-$LiClO_4$ exhibits a better interfacial stability with lithium metal than PEO-$LiClO_4$. Therefore, the high ionic conductivity, high lithium-ion transference number, wide electrochemical stability window and better interfacial stability with lithium metal make CPR500-$LiClO_4$ a suitable SPE for all-solid-state lithium batteries.

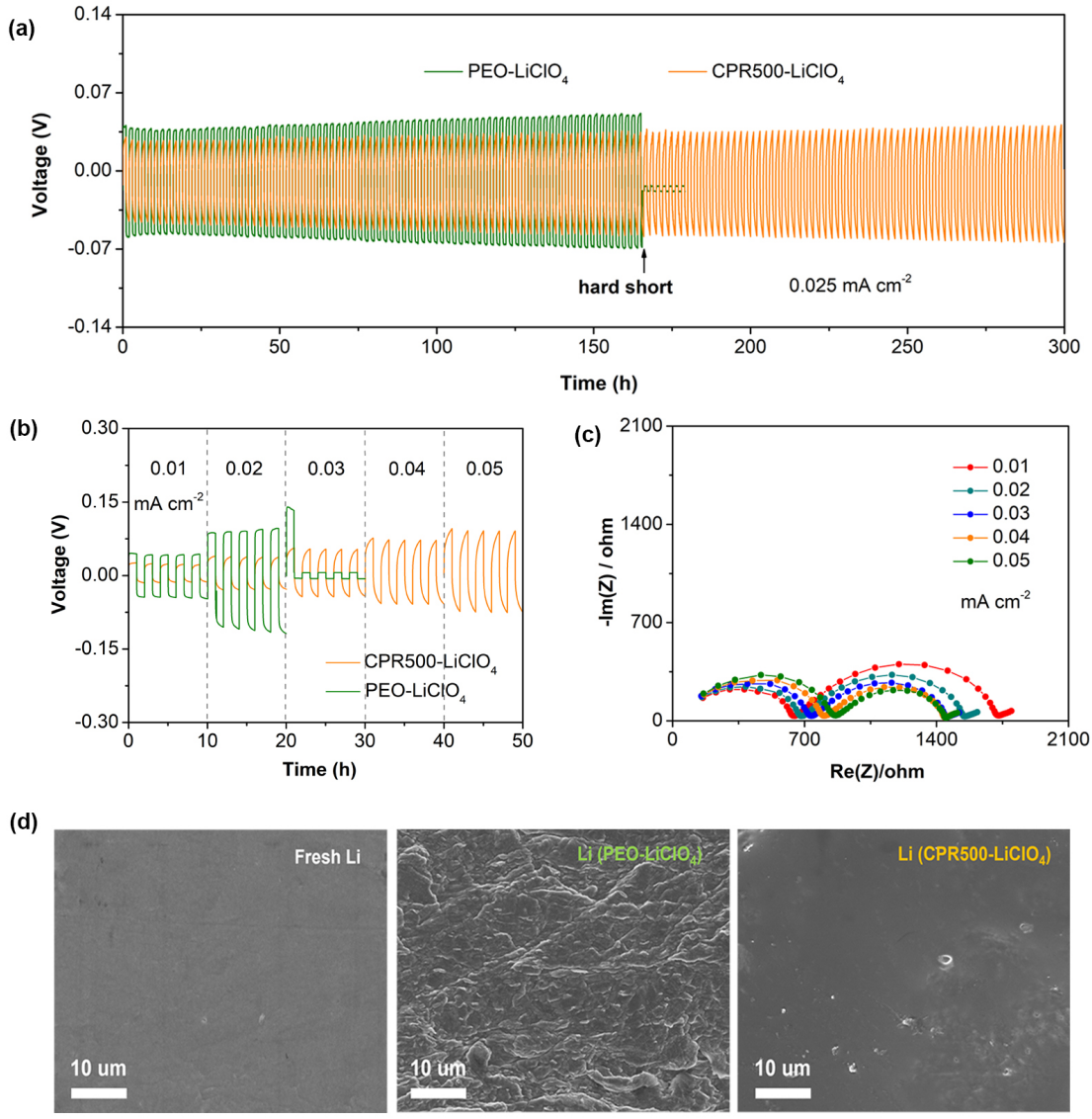

Figure 4. Galvanostatic cycling curves of the Li||PEO-$LiClO_4$||Li and Li||CPR500-$LiClO_4$||Li cells at (a) the constant current density of 0.025 mA cm^{-2} and (b) different current densities from 0.01 to 0.05 mA cm^{-2} at 60 °C. (c) The initial and final EIS curves at different current densities of Li||CPR500-$LiClO_4$||Li cell at 60 °C. (d) SEM

images of the fresh Li and Li anodes obtained from Li||PEO-$LiClO_4$||Li and Li||CPR500-$LiClO_4$||Li symmetric cells after running for 300 h at the current density of 0.025 mA cm^{-2}.

To assemble all-solid state lithium metal batteries, cathodes should be formulated with a catholyte to ensure ionic conduction inside the cathode materials and good interfacial contact with the SPE membranes. Therefore, CPR500-$LiClO_4$ and CPR2000-$LiClO_4$ as well as reference PEO-$LiClO_4$ have been investigated as potential catholytes for cathode fabrication together with LFP as electroactive cathode material and conducting carbon additives. This has led to three types of cathodes, namely LFP500, LFP2000 and LFP600K cathodes in which catholytes are CPR500-$LiClO_4$, CPR2000-$LiClO_4$ and PEO-$LiClO_4$, respectively. Figures 5a-c show the charge and discharge voltage profiles of cells with LFP600K, LFP500 and LFP2000 cathodes at various rates from 0.1 to 1 C in the voltage range from 3.0 to 3.8 V at 60 °C. For all the investigated cells, a CPR500-$LiClO_4$ SPE membrane was used. The cells with LFP500 and LFP2000 cathodes exhibit flat charge and discharge platforms and the gaps between the charge and discharge platforms are small, indicating small voltage polarization. The small voltage polarization of the cell based on the LFP2000 cathode originates from the high lithium-ion diffusion coefficients, which is evidenced by the GITT test. Among the different cells, the cell with the LFP2000 cathode shows the highest initial discharge capacity at the same current density. As illustrated in Figure 5d, the LFP2000 based cell shows the highest discharge capacities at different current densities with better cycling stability, which are 167.8, 144.2, 94.8 and 60.2 mAh g^{-1} at 0.1, 0.2, 0.5 and 1C.

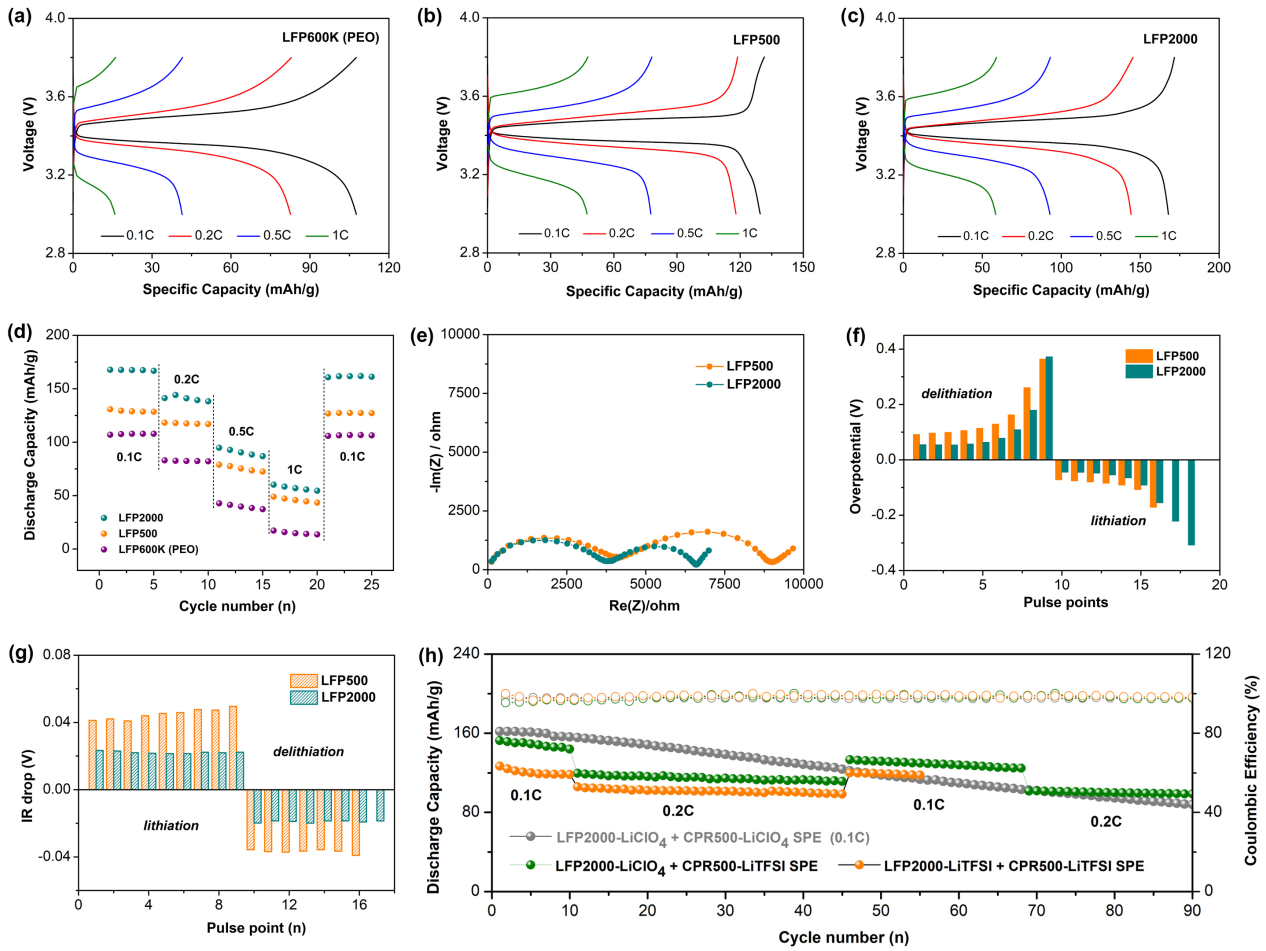

Figure 5. (a-c) Charge and discharge voltage profiles of full cells with the LFP600K, LFP500 and LFP2000 cathodes at various rates. (d) Rate performances of full cells with the LFP600K, LFP500 and LFP2000 cathodes. (e) EIS plots of full cells with LFP500 and LFP2000 cathodes after GITT test. (f) Overpotentials and (g) IR drops of full cells with LFP500 and LFP2000 cathodes calculated from GITT during the lithiation and delithiation processes, respectively. (h) Long cycling stability of full cells with LFP2000 cathodes and CPR500 SPEs.

EIS was performed to evaluate the interface kinetics in the full cells with LFP500 and LFP2000 cathodes after GITT test. As shown in Figure 5e, the two cells with LFP500 and LFP2000 cathodes exhibit two semicircles. The semicircles represent the bulk resistance of the solid polymer electrolyte in the higher frequency range and interfacial resistance in the lower frequency range.[54] Since CPR500-$LiClO_4$ is used as SPE for the cells made of LFP500 and LFP2000

cathodes, both cells exhibit the bulk resistance of the CPR500-$LiClO_4$ SPE. However, the interfacial resistance of the LFP2000 cell is much smaller than that of the LFP500 one, which could be due to a more effectively filling of the inter-particulate spaces, as shown in Figure S7, indicating a better binder behavior for CPR2000 compared to CPR500. This could be related to the mechanical properties of the CPR2000 and CPR500 which have revealed a stiffer network in case of CPR500, while a softer network was formed by CPR2000. This was attributed to the longer PEG segments found in CPR2000, which could promote in turn excellent flexibility and binder behavior to this sample. CPR2000 could connect LFP particles forming ion-conducting pathways, which can increase the bulk ionic conductivity of the LFP2000 cathode.[55] Therefore, the interfacial resistance of the cell made with LFP2000 is much smaller than that of LFP500. As shown in capacity versus cell voltage (dQ_m/dV) plots (Figures S8a-c), the variation of the redox potentials also confirms the small voltage polarization during the charge and discharge processes for LFP2000 cathodes.[56] In addition, the Li^+ diffusion coefficients (D_{Li}) in LFP500 and LFP2000 cathodes were investigated through the GITT test. Figures S9a-b show GITT plots of cells with LFP500 and LFP2000 during the lithiation and delithiation processes. In Figure S9c, the calculated D_{Li} of LFP2000 is 5.61×10^{-15} cm^2 s^{-1} for both the lithiation and delithiation processes, which is a little higher than that of LFP500 (3.77×10^{-15} cm^2 s^{-1}). As shown in Figures 5f-g, the overpotential and IR drop (sudden voltage step owing to the current flux) of the cell with LFP2000 are also lower than that of LFP500, further suggesting the better electrochemical reaction kinetics of LFP2000 cathode.[57, 58] Therefore, the small voltage polarization and better electrochemical reaction kinetics as well as high lithium-ion diffusion coefficients make LFP2000 a suitable cathode for all-solid-state lithium metal batteries. As final experiment, the long-term cycling stability of the full

cell made with LFP2000-$LiClO_4$ cathode and the CPR500-$LiClO_4$ SPE was investigated as shown in Figure 5h. The initial discharge capacity is around 160 mAh g^{-1}. After 90 cycles, this cell delivers a discharge capacity near to 90 mAh g^{-1} and displays a high coulombic efficiency of 98% at 0.1 C at 60 ℃. The 0.51% capacity loss per cycle is attributed to the unstable SEI formation on the lithium surface.

XPS was carried out to study the chemical components on the surfaces of the lithium anode after cycling. Figure 6a show the XPS C1s spectrum recorded on the lithium anode surfaces for CPR500-$LiClO_4$. The peak at 286.4 eV belongs to the $–CH_2–O–$ of PEO and the peak at 284.8 eV is attributed to $-CH_2–$, which is consistent with the result of the literature.[59] The O1s spectrum in Figure 6b exhibits two peaks including $–CH_2–O–$ and Li_2O at 532.8 and 530.5 eV, respectively.[60, 61] The signal of Li_2O was also found in the Li1s spectrum, which is shown in Figure 6c. As exhibited in Figure 6d, the peak at higher binding energy (206-211 eV) in the Cl2p spectrum indicates the presence of $LiClO_4$ salt. However, in addition to $LiClO_4$ salt, the Cl 2p peak at lower binding energy (196-202 eV) can be assigned to LiCl, suggesting that decomposition of $LiClO_4$ was observed on the surface of the Li anode.[62] These results clearly demonstrate that the decomposition products of $LiClO_4$ (Li_2O and LiCl) in CPR500-$LiClO_4$ electrolyte are present on the surface of lithium anode and these products constitute the solid electrolyte interface (SEI). According to XPS analysis, the decomposition of $LiClO_4$ results in the unstable SEI on the lithium anodes, further leading to capacity decay of full cell.

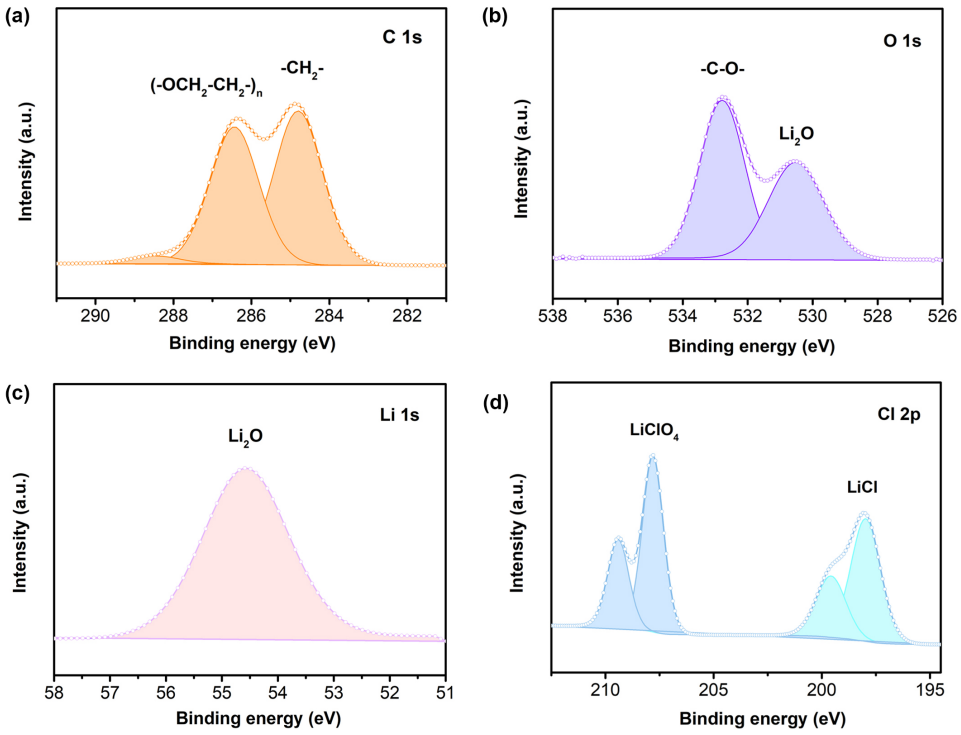

Figure 6. (a) C 1s, (b) O 1s, (c) Li 1s and Cl 2p XPS spectra of the Li anodes using CPR500-$LiClO_4$ membrane after cycling.

The influence of lithium salts on the electrochemical performance of all solid-state lithium-ion batteries has been investigated. As shown in Figure S11, compared to solid polymer electrolyte containing LiTFSI, the electrolyte containing $LiClO_4$ exhibited significantly higher overpotential in Li-Li symmetric cells under higher current density conditions, and when the current density exceeds 0.05 mA cm^{-2}, the battery failed due to excessive overpotential. This corresponds to the widening of the charge-discharge plateau separation during the full battery cycling process due to the polarization (Figure S12). In comparison with CPR500-$LiClO_4$, thanks to the formation of more stable SEI layer, the CPR500-LiTFSI endures higher current density until 0.10 mA cm^{-2}. Therefore, the CPR500-LiTFSI shows better stability with lithium metal because it can stand higher current density. The CPR500-LiTFSI was used as SPE in the full cell and the electrochemical performance was studied. Figure 5h also shows the long cycling stability of full cells with CPR500-LiTFSI SPE

at various rates at 60 °C. The full cell with LFP2000-LiTFSI cathode and CPR500-LiTFSI SPE shows the lowest discharge capacities of 124.1 and 118.4 mAh g^{-1} of 1st and 10th at 0.1C as well as 105.8, 102.2, 101.4 and 100.1 mAh g^{-1} of 1st, 10th, 20th and 30th at 0.2 C compared with the other two compositions. However, the full cell with LFP2000-$LiClO_4$ cathode and CPR500-LiTFSI SPE shows a higher discharge capacities of 152.6 and 143.9 mAh g^{-1} of 1st and 10th at 0.1C as well as 119.5, 116.2, 114.6 and 113.0 mAh g^{-1} of 1st, 10th, 20th and 30th at 0.2 C. Moreover, after 55 cycles, the full cell with LFP2000-LiTFSI cathode and CPR500-LiTFSI SPE delivers a discharge capacity near to 120 mAh g^{-1} at 0.1 C, which is already higher than that of full cell with LFP2000-$LiClO_4$ cathode and the CPR500-$LiClO_4$ SPE (113.5 mAh g^{-1}) at the same rate. It is worth noting that the full cell with LFP2000-$LiClO_4$ cathode and CPR500-LiTFSI SPE displays a discharge capacity near to 100 mAh g^{-1} when it backs to 0.2 C after 90 cycles, which is much higher than that of full cell with LFP2000-$LiClO_4$ cathode and the CPR500-$LiClO_4$ SPE (near to 90 mAh g^{-1}) at 0.1C. Furthermore, this cycling performance was achieved under continuous alternating cycling conditions between 0.1C and 0.2C rates, without compromising cycling stability (the capacity decay of the full cell improves from 0.51 % per cycle at 0.1 C to 0.13 % per cycle at 0.2C), when the $LiClO_4$ was changed by LiTFSI in the electrolyte. Nevertheless, due to the higher ionic conductivity and lower activation energy of the electrolyte when $LiClO_4$ is used as the added lithium salt, the assembled full battery exhibits a higher initial capacity.

4. Conclusions

Novel modified polyrotaxane polymer networks, CPR500 and CPR2000, were prepared, in which poly(ethylene glycol) diglycidyl ethers with different molar masses (M_n=500 and 2000) were

used as crosslinkers. ^{1}H NMR, FTIR and rheological tests confirmed the network structure for CPR500 and CPR2000. Both networks exhibit good thermal stability until 200 ℃. Crystallization is more pronounced in the CPR2000 sample because it contains longer PEG segments but is further decreased in both samples after addition of $LiClO_4$. The CPR500 sample forms a stiffer network and, after loading with an optimal amount of $LiClO_4$ with an EO/Li^+ molar ratio of 10:1, showing a high ionic conductivity of 7.25×10^{-4} S cm^{-1}, a lithium-ion transference number of 0.54 and a wide electrochemical stability window from 1.6 to 5.0 V (*vs.* Li^+/Li) at 60 ℃. This further allows the use of CPR500-$LiClO_4$ membranes as SPEs for all-solid-state lithium metal batteries. The CPR2000 sample exhibits excellent binding properties and has been employed as catholytes for cathode fabrication. The LFP2000 cathode exhibits the smaller voltage polarization, the better electrochemical reaction kinetics as well as high lithium-ion diffusion coefficients allowing its use in an all-solid-state lithium battery. The accordingly prepared LFP2000||CPR500-$LiClO_4$||Li cell can achieve a high discharge capacity over 160 mAh g^{-1} at 0.1 C at 60 ℃. The cell with CPR2000 catholyte also exhibits much better cycling performance than the other combinations including PEO catholyte. When LiTFSI and $LiClO_4$ are respectively chosen as lithium salt additives in the electrolyte and cathode, paired with different cross-linking structures of polymer matrices, the all-solid-state battery exhibits a slight decrease in initial capacity and a significant improvement in cycling stability (alternating cycling between 0.1C and 0.2C rates, single-cycle capacity loss of 0.13%). This work provides new polymer structure options for all-solid-state polymer batteries from catholytes to electrolytes. Furthermore, it validates the customization of designs tailored to the differing material properties required by the electrolyte and cathode, resulting in a significant enhancement in both capacity and cycling stability of the entire battery.

Supporting Information

^{1}H NMR spectra of α-CDs/PEG-COOH and PRX (d6-DMSO, 300 MHz); ^{1}H NMR spectra of PRX, CPR500, CPR2000 and the partial enlargement of spectra (d6-DMSO, 300 MHz); Frequency sweep tests of CPR500 and CPR2000 at different temperatures; DSC curve of PRX; Dynamic frequency sweep curves of CPR500 and CPR500-$LiClO_4$ at 60, 80 and 100 ℃; DSC curves of CPR500 and CPR500-$LiClO_4$; Storage modulus-temperature curve of CPR500-$LiClO_4$; Arrhenius plots of the ionic conductivity for CPR2000-$LiClO_4$; SEM images of LFP500 and LFP2000; The dQ/dV profiles of LFP500 and LFP2000 of the second charge and discharge process at 1C; The difference of oxidation and reduction peaks of LFP500 and LFP2000 for 5 cycles at 1C; Schematic illustration for a single step of a GITT titration during lithiation and delithiation process; D_{Li} of LFP500 and LFP2000 calculated from GITT during the lithiation and delithiation processes, respectively; Galvanostatic cycling curves of the Li||CPR500-$LiClO_4$||Li cell at different current densities from 0.06 to 0.10 mA cm^{-2} at 60 ℃; Galvanostatic cycling curves of the Li||CPR500-LiTFSI||Li cell at different current densities from 0.01 to 0.10 mA cm^{-2} at 60 ℃; Charge and discharge voltage profiles of full cells with the LFP2000 cathode at different cycles; The composition of the cathode; The electrochemical performance of solid state electrolytes based on the pseudo-polyrotaxanes including ionic conducvity (σ), lithium ion transference number (t_{Li^+}) and electrochemical stability window (ESW); The free ClO_4^- anion versus the contact $Li^+ClO_4^-$ ion pair ratio indicating the degree of dissociation of $LiClO_4$ in CPR500-$LiClO_4$ with different ratios of ether group and lithium ions.

Corresponding Author

Jean-François Gohy – Institute of Condensed Matter and Nanoscience (IMCN), Bio- and Soft Matter (BSMA), Université catholique de Louvain, Place L. Pasteur, 1, 1348, Louvain-la-Neuve, Belgium; Email: jean-francois.gohy@uclouvain.be

He Jia – Institute of Condensed Matter and Nanoscience (IMCN), Bio- and Soft Matter (BSMA), Université catholique de Louvain, Place L. Pasteur, 1, 1348, Louvain-la-Neuve, Belgium; Email: he.jia@uclouvain.be

Author Contributions

The manuscript was written through contributions of all authors. All authors have given approval to the final version of the manuscript.

Declaration of Competing Interest

The authors declare that they have no known competing financial interests or personal relationships that could have appeared to influence the work reported in this paper.

Acknowledgements

S. Y., Z. C. and Z. H. acknowledge the China Scholarship Council. S.Y. thanks Dr. He Jia and Dr. Rowanne Lyons for their kind help for the polyrotaxane synthesis. S.Y. is also grateful to Dr. Yanzhao Li and Dr. Hao Wang for their kind help about polymer electrolyte preparation, rheology test and analysis.

References

[1] A. Masias, J. Marcicki, W.A. Paxton, Opportunities and Challenges of Lithium Ion Batteries in Automotive Applications, ACS Energy Lett. 6 (2) (2021) 621-630. https://doi.org/10.1021/acsenergylett.0c02584.

[2] J. Yu, X. Lin, J. Liu, J.T.T. Yu, M.J. Robson, G. Zhou, H.M. Law, H. Wang, B.Z. Tang, F. Ciucci, In situ fabricated quasi-solid polymer electrolyte for high-energy-density lithium metal battery capable of subzero operation, Adv. Energy Mater. 12 (2) (2021) 2102932. https://doi.org/10.1002/aenm.202102932.

[3] F. Lv, Z. Wang, L. Shi, J. Zhu, K. Edström, J. Mindemark, S. Yuan, Challenges and development of composite solid-state electrolytes for high-performance lithium ion batteries, J. Power Sources 441 (2019) 227175. https://doi.org/10.1016/j.jpowsour.2019.227175.

[4] Y. Lin, M. Wu, J. Sun, L. Zhang, Q. Jian, T. Zhao, A high-capacity, long-cycling all-solid-state lithium battery enabled by integrated cathode/ultrathin solid electrolyte, Adv. Energy Mater. 11 (35) (2021) 2101612. https://doi.org/10.1002/aenm.202101612.

[5] R. Li, J. Li, L. Li, H. Yang, G. Zhang, J. Xiang, X. Shen, M. Jing, A bifunctional composite artificial solid electrolyte interphase for high stable solid-state lithium batteries, Colloid Surface A 657 (2023) 130600. https://doi.org/10.1016/j.colsurfa.2022.130600.

[6] Q. Hu, Z. Sun, L. Nie, S. Chen, J. Yu, W. Liu, High-safety composite solid electrolyte based on inorganic matrix for solid-state lithium-metal batteries, Mater. Today Energy 27 (2022) 101052. https://doi.org/10.1016/j.mtener.2022.101052.

[7] H. Yang, B. Zhang, M. Jing, X. Shen, L. Wang, H. Xu, X. Yan, X. He, In situ catalytic polymerization of a highly homogeneous PDOL composite electrolyte for long-cycle high-voltage solid-state lithium batteries, Adv. Energy Mater. 12 (39) (2022) 2201762. https://doi.org/10.1002/aenm.202201762.

[8] H. Wu, R. Li, J. Li, L. Zhou, Y. Liu, G. Zhang, M. Jing, An in-situ synergistic enhancement strategy from g-C_3N_4 and PDOL composite solid electrolyte on the interface stability of solid-state lithium battery, Surf. Interfaces. 46 (2024) 104048. https://doi.org/10.1016/j.surfin.2024.104048.

[9] H. Yang, M. Jing, H. Li, W. Yuan, B. Deng, Q. Liu, B. Ju, X. Zhang, S. Hussain, X. Shen, X. Yan, 'Environment-friendly' polymer solid electrolyte membrane via a rapid surface-initiating polymeration strategy, Chem. Eng. J. 421 (2021) 129710. https://doi.org/10.1016/j.cej.2021.129710.

[10] H. Yang, M. Jing, L. Wang, H. Xu, X. Yan, X. He, PDOL-based solid electrolyte toward practical application: opportunities and challenges, Nano-micro Lett. 16 (127) (2024) 1-33. https://doi.org/10.1007/s40820-024-01354-z.

[11] Y. An, X. Han, Y. Liu, A. Azhar, J. Na, A.K. Nanjundan, S. Wang, J. Yu, Y. Yamauchi, Progress in solid polymer electrolytes for lithium-ion batteries and beyond, Small 18 (3) (2022) 2103617. https://doi.org/10.1002/smll.202103617.

[12] T. H. Mengesha, S. L. Beshahwured, Y. S. Wu, S. H. Wu, R. Jose, C. C. Yang, A polydopamine-modified garnet–based polymer-in-ceramic hybrid solid electrolyte membrane for high-safety lithium metal batteries, Chem. Eng. J. 452 (2023) 139340. https://doi.org/10.1016/j.cej.2022.139340.

[13] Y. C. Wang, R. Maeda, G. Kali, H. Yokoyama, G. Wenz, K. Ito, Synthesis of poly(methylmethacrylate)-based polyrotaxane via reversible addition-fragmentation chain transfer polymerization, ACS Macro Lett. 9 (12) (2020) 1853-1857. https://doi.org/10.1021/acsmacrolett.0c00648.

[14] L. Y. Yang, D. X. Wei, M. Xu, Y. F. Yao, Q. Chen, Transferring lithium ions in nanochannels: a PEO/Li^+ solid polymer electrolyte design, Angew. Chem. Int. Ed. 53 (14) (2014) 3631-3635. https://doi.org/10.1002/anie.201307423.

[15] L. Imholt, T. S. Dörr, P. Zhang, L. Ibing, I. Cekic-Laskovic, M. Winter, G. Brunklaus, Grafted polyrotaxanes as highly conductive electrolytes for lithium metal batteries, J. Power Sources 409 (2019) 148-158. https://doi.org/10.1016/j.jpowsour.2018.08.077.

[16] Y. C. Lin, K. Ito, H. Yokoyama, Solid polymer electrolyte based on crosslinked polyrotaxane, Polymer 136 (2018) 121-127. https://doi.org/10.1016/j.polymer.2017.12.046.

[17] Y. He, Y. Li, Q. Tong, J. Zhang, J. Weng, M. Zhu, Highly conductive and thermostable grafted polyrotaxane/ceramic hybrid polymer electrolyte for solid-state lithium-metal batteries, ACS Appl. Mater. Interfaces 13 (35) (2021) 41593-41599. https://doi.org/10.1021/acsami.1c10232.

[18] H. Al-Salih, M.S.E. Houache, E.A. Baranova, Y. Abu-Lebdeh, Composite cathodes for solid-state lithium batteries: “Catholytes” the underrated giants, Adv. Energy Sustainability Res. 3 (8) (2022) 2200032. https://doi.org/10.1002/aesr.202200032..

[19] M. Wetjen, G. T. Kim, M. Joost, G. B. Appetecchi, M. Winter, S. Passerini, Thermal and electrochemical properties of PEO-LiTFSI-Pyr_{14}TFSI-based composite cathodes, incorporating 4 V-class cathode active materials, J. Power Sources. 246 (2014) 846-857. https://doi.org/10.1016/j.jpowsour.2013.08.037.

[20] I. Aldalur, H. Zhang, M. Piszcz, U. Oteo, L. M. Rodriguez-Martinez, D. Shanmukaraj, T. Rojo, M. Armand, Jeffamine® based polymers as highly conductive polymer electrolytes and cathode binder materials for battery application, J. Power Sources. 347 (2017) 37-46. https://doi.org/10.1016/j.jpowsour.2017.02.047.

[21] Y. C. Jung, S. M. Lee, J. H. Choi, S. S. Jang, D. W. Kim, All solid-state lithium batteries assembled with hybrid solid electrolytes, J. Electrochem. Soc. 162 (4) (2015) 704-710. https://doi.org/10.1149/2.0731504jes.

[22] Y. C. Jung, M. S. Park, C. H. Doh, D. W. Kim, Organic-inorganic hybrid solid electrolytes for solid-state lithium cells operating at room temperature, Electrochim. Acta. 218 (2016) 271-277. https://doi.org/10.1016/j.electacta.2016.09.141.

[23] J. H. Choi, C. H. Lee, J. H. Yu, C. H. Doh, S. M. Lee, Enhancement of ionic conductivity of composite membranes for all-solid-state lithium rechargeable batteries incorporating tetragonal $Li_7La_3Zr_2O_{12}$ into a polyethylene oxide matrix, J. Power Sources. 274 (2015) 458-463. https://doi.org/10.1016/j.jpowsour.2014.10.078.

[24] L. Li, H. Duan, J. Li, L. Zhang, Y. Deng, G. Chen, Toward high performance all-solid-state lithium batteries with high-voltage cathode materials: design strategies for solid electrolytes, cathode interfaces and composite electrodes, Adv. Energy Mater. 11 (28) (2021) 2003154. https://doi.org/https://doi.org/10.1002/aenm.202003154.

[25] L. F. Hart, J. E. Hertzog, P. M. Rauscher, B. W. Rawe, M. M. Tranquilli, S. J. Rowan, Material properties and applications of mechanically interlocked polymers, Nat. Rev. Mater. 6 (6) (2021) 508-530. https://doi.org/10.1038/s41578-021-00278-z.

[26] Y. Kobayashi, Precise synthesis of polyrotaxane and preparation of supramolecular materials based on its mobility, Polym J 53 (4) (2021) 505-513. https://doi.org/10.1038/s41428-020-00455-x.

[27] J. Araki, C. Zhao, K. Ito, Efficient production of polyrotaxanes from α-cyclodextrin and poly(ethylene glycol), Macromolecules 38 (17) (2005) 7524-7527. https://doi.org/10.1021/ma050290+.

[28] S. Liu, C. Zhong, W. Wang, Y. Jia, L. Wang, L. Ren, α-cyclodextrins polyrotaxane loading silver sulfadiazine, Polymers 10 (2) (2018) 190. https://doi.org/10.3390/polym10020190.

[29] K. Kato, Y. Okabe, Y. Okazumi, K. Ito, A significant impact of host-guest stoichiometry on the extensibility of polyrotaxane gels, Chem. Commun. 51 (90) (2015) 16180-16183. https://doi.org/10.1039/c5cc07122d.

[30] M. Chen, Q. Dong, W. Ni, X. Zhao, Q. Gu, G. Tang, D. Li, W. Ma, Z. Hou, Cyclodextrin-based polymer-assisted Ru nanoparticles for the aqueous hydrogenation of biomass-derived platform molecules, ChemistrySelect 2 (32) (2017) 10537-10545. https://doi.org/10.1002/slct.201702229.

[31] R. Zhao, T. Tan, C. Sandstrom, NMR studies on puerarin and its interaction with beta-cyclodextrin, J. Biol. Phys. 37 (4) (2011) 387-400. https://doi.org/10.1007/s10867-011-9221-0.

[32] M. P. Kapoor, M. Moriwaki, K. Minoura, D. Timm, A. Abe, K. Kito, Structural investigation of hesperetin-7-O-glucoside inclusion complex with β-cyclodextrin: a spectroscopic assessment, Molecules 27 (17) (2022) 5395. https://doi.org/10.3390/molecules27175395.

[33] Z. Liu, L. Ye, J. Xi, J. Wang, Z. Feng, Cyclodextrin polymers: structure, synthesis, and use as drug carriers, Prog. Polym. Sci. 118 (2021) 101408. https://doi.org/10.1016/j.progpolymsci.2021.101408.

[34] W. J. Liang, Y. P. Chen, C. P. Wu, P. L. Kuo, Solid polymer electrolytes. XI. Preparation, characterization and ionic conductivity of new plasticized polymer electrolytes based on chemical-covalent polyether-siloxane hybrids, J. Appl. Polym. Sci. 100 (2) (2006) 1000-1007. https://doi.org/10.1002/app.22827.

[35] G. Stojkov, Z. Niyazov, F. Picchioni, R. K. Bose, Relationship between structure and rheology of hydrogels for various applications, Gels 7 (4) (2021) 255. https://doi.org/10.3390/gels7040255.

[36] T. J. Singh, S. V. Bhat, Morphology and conductivity studies of a new solid polymer electrolyte: $(PEG)_xLiClO_4$, Bull. Mater. Sci. 26 (2003) 707-714. https://doi.org/10.1007/BF02706768.

[37] W. A. Henderson, Crystallization kinetics of glyme-LiX and PEO-LiX polymer electrolytes, Macromolecules 40 (14) (2007) 4963-4971. https://doi.org/10.1021/ma061866d.

[38] V. St-Onge, M. Cui, S. Rochon, J. C. Daigle, J.P. Claverie, Reducing crystallinity in solid polymer electrolytes for lithium-metal batteries via statistical copolymerization, Commun. Mater. 2 (1) (2021) 83. https://doi.org/10.1038/s43246-021-00187-2.

[39] J. L. Olmedo-Martinez, L. Meabe, A. Basterretxea, D. Mecerreyes, A. J. Muller, Effect of chemical structure and salt concentration on the crystallization and ionic conductivity of aliphatic polyethers, Polymers 11 (3) (2019) 452. https://doi.org/10.3390/polym11030452.

[40] L. Bai, S. Ghiassinejad, J. Brassinne, Y. Fu, J. Wang, H. Yang, A. Vlad, A. Minoia, R. Lazzaroni, J. F. Gohy, High salt-content plasticized flame-retardant polymer electrolytes, ACS Appl. Mater. Interfaces 13 (37) (2021) 44844-44859. https://doi.org/10.1021/acsami.1c11058.

[41] J. L. Olmedo-Martínez, L. Porcarelli, G. Guzmán-González, I. Calafel, M. Forsyth, D. Mecerreyes, A. J. Müller, Ternary poly(ethylene oxide)/poly(L,L-lactide) PEO/PLA blends as high-temperature solid polymer electrolytes for lithium batteries, ACS Appl. Polym. Mater. 3 (12) (2021) 6326-6337. https://doi.org/10.1021/acsapm.1c01093.

[42] G. Homann, L. Stolz, K. Neuhaus, M. Winter, J. Kasnatscheew, Effective optimization of high voltage solid-state lithium batteries by using poly(ethylene oxide)-based polymer electrolyte with semi-interpenetrating network, Adv. Funct. Mater. 30 (46) (2020) 2006289. https://doi.org/10.1002/adfm.202006289.

[43] Z. Chen, H. Jia, S. Yan, J. F. Gohy, Polymer-coated silica dual functional fillers to improve the performance of poly(ethylene oxide)-based solid electrolytes, Nano Energy 114 (2023) 108637. https://doi.org/10.1016/j.nanoen.2023.108637.

[44] R. Bakar, S. Darvishi, U. Aydemir, U. Yahsi, C. Tav, Y.Z. Menceloglu, E. Senses, Decoding polymer architecture effect on ion clustering, chain dynamics and ionic conductivity in polymer electrolytes, ACS Appl. Energy Mater 6 (7) (2023) 4053-4064. https://doi.org/10.1021/acsaem.3c00310.

[45] L. Matkovska, M. Iurzhenko, Y. Mamunya, I. Tkachenko, V. Demchenko, V. Synyuk, A. Shadrin, G. Boiteux, Structural peculiarities of ion-conductive organic-inorganic polymer composites based on aliphatic epoxy resin and salt of lithium perchlorate, Nanoscale Res. Lett. 12 (1) (2017) 423. https://doi.org/10.1186/s11671-017-2195-5.

[46] X. Cai, J. Ding, Z. Chi, W. Wang, D. Wang, G. Wang, Rearrangement of ion transport path on nano-cross-linker for all-solid-state electrolyte with high room temperature ionic conductivity, ACS Nano 15 (12) (2021) 20489-20503. https://doi.org/10.1021/acsnano.1c09023.

[47] J. Seo, G. H. Lee, J. Hur, M. C. Sung, J. H. Seo, D. W. Kim, Mechanically interlocked polymer electrolyte with built-In fast molecular shuttles for all-solid-state lithium batteries, Adv. Energy Mater. 11 (44) (2021) 2102583. https://doi.org/10.1002/aenm.202102583.

[48] D. Lin, W. Liu, Y. Liu, H. R. Lee, P. C. Hsu, K. Liu, Y. Cui, High ionic conductivity of composite solid polymer electrolyte via in situ synthesis of monodispersed SiO_2 nanospheres in poly(ethylene oxide), Nano Lett. 16 (1) (2016) 459-465. https://doi.org/10.1021/acs.nanolett.5b04117.

[49] S. H. S. Cheng, K. Q. He, Y. Liu, J. W. Zha, M. Kamruzzaman, R. L. W. Ma, Z. M. Dang, R. K. Y. Li, C. Y. Chung, Electrochemical performance of all-solid-state lithium batteries using inorganic lithium garnets particulate reinforced PEO/$LiClO_4$ electrolyte, Electrochim. Acta. 253 (2017) 430-438. https://doi.org/10.1016/j.electacta.2017.08.162.

[50] X. W Zhang, C. Wang, A. J. Appleby, F. E. Little, Characteristics of lithium-ion-conducting composite polymer-glass secondary cell electrolytes, J. Power Sources. 112 (1) (2002) 209-215. https://doi.org/10.1016/S0378-7753(02)00365-8.

[51] X. Fu, Y. Li, C. Liao, W. Gong, M. Yang, R. K. Y. Li, S. C. Tjong, Z. Lu, Enhanced electrochemical performance of solid PEO/$LiClO_4$ electrolytes with a 3D porous $Li_{6.28}La_3Zr_2Al_{0.24}O_{12}$ network, Comp. Sci. Technol. 184 (2019) 107863. https://doi.org/10.1016/j.compscitech.2019.107863.

[52] X. Zhang, J. Xie, F. Shi, D. Lin, Y. Liu, W. Liu, A. Pei, Y. Gong, H. Wang, K. Liu, Y. Xiang, Y. Cui, Vertically aligned and continuous nanoscale ceramic-polymer interfaces in composite solid polymer electrolytes for enhanced ionic conductivity, Nano Lett. 18 (6) (2018) 3829-3838. https://doi.org/10.1021/acs.nanolett.8b01111.

[53] K. Chen, R. Pathak, A. Gurung, E. A. Adhamash, B. Bahrami, Q. He, H. Qiao, A. L. Smirnova, J. J. Wu, Q. Qiao, Y. Zhou, Flower-shaped lithium nitride as a protective layer via facile plasma activation for stable lithium metal anodes, Energy Stor. Mater. 18 (2019) 389-396. https://doi.org/10.1016/j.ensm.2019.02.006.

[54] J. Zheng, C. Sun, Z. Wang, S. Liu, B. An, Z. Sun, F. Li, Double ionic-electronic transfer interface layers for all-solid-state lithium batteries, Angew. Chem. Int. Ed. 60 (34) (2021) 18448-18453. https://doi.org/https://doi.org/10.1002/anie.202104183.

[55] S. Cho, S. Kim, W. Kim, S. Kim, S. Ahn, All-solid-state lithium battery working without an additional separator in a polymeric electrolyte, Polymers 10 (12) (2018) 1364. https://doi.org/10.3390/polym10121364.

[56] W. Chen, X. Xiong, R. Zeng, L. Jiang, Z. Chen, Z. Xiao, L. Qie, F. Yu, Y. Huang, Enhancing the interfacial ionic transport via in situ 3D composite polymer electrolytes for solid-state lithium batteries, ACS Appl. Energy Mater. 3 (7) (2020) 7200-7207. https://doi.org/10.1021/acsaem.0c01269.

[57] J. Kim, S. Park, S. Hwang, W. S. Yoon, Principles and applications of galvanostatic intermittent titration technique for lithium-ion batteries, J. Electrochem. Sci. Technol. 13 (1) (2022) 19-31. https://doi.org/10.33961/jecst.2021.00836.

[58] F. Wang, B. Wang, T. Ruan, T. Gao, R. Song, F. Jin, Y. Zhou, D. Wang, H. Liu, S. Dou, construction of structure-tunable Si@Void@C anode materials for lithium-ion batteries through controlling the growth kinetics of resin, ACS Nano 13 (10) (2019) 12219-12229. https://doi.org/10.1021/acsnano.9b07241.

[59] C. Xin, K. Wen, S. Guan, C. Xue, X. Wu, L. Li, C. W. Nan, A cross-linked poly(ethylene oxide)-based electrolyte for all-solid-state lithium metal batteries with long cycling stability, Front. Mater. 9 (2022) 864478. https://doi.org/10.3389/fmats.2022.864478.

[60] K. N. Wood, K. X. Steirer, S. E. Hafner, C. Ban, S. Santhanagopalan, S. H. Lee, G. Teeter, Operando X-ray photoelectron spectroscopy of solid electrolyte interphase formation and evolution in Li_2S-P_2S_5 solid-state electrolytes, Nat. Commun. 9 (1) (2018) 2490. https://doi.org/10.1038/s41467-018-04762-z.

[61] K. N. Wood, G. Teeter, XPS on Li-Battery-Related Compounds: Analysis of inorganic SEI phases and a methodology for charge correction, ACS Appl. Energy Mater. 1 (9) (2018) 4493-4504. https://doi.org/10.1021/acsaem.8b00406.

[62] R. Younesi, M. Hahlin, K. Edstrom, Surface characterization of the carbon cathode and the lithium anode of Li-O_2 batteries using $LiClO_4$ or LiBOB salts, ACS Appl. Mater. Interfaces 5 (4) (2013) 1333-1341. https://doi.org/10.1021/am3026129.